Materials Advances

ROYAL SOCIETY OF CHEMISTRY

PAPER

View Article Online
View Journal | View Issue

Check for updates

Cite this: *Mater. Adv.*, 2022, 3, 1087

Crystal field-induced lattice expansion upon reversible oxygen uptake/release in $YbMn_xFe_{2-x}O_4$†

Tianyu Li,[a] Rishvi Jayathilake,[a] Lahari Balisetty,[a] Yuan Zhang,[a] Brandon Wilfong,[ab] Timothy J. Diethrich [a] and Efrain E. Rodriguez *[ab]

Received 7th September 2021,
Accepted 17th November 2021

DOI: 10.1039/d1ma00822f

rsc.li/materials-advances

We successfully form the solid solutions $YbMn_xFe_{2-x}O_4$ for x = 0.25, 0.50, 0.75, and 1.0 in order to study the mechanism of oxygen release and uptake as a function of Mn substitution. High-resolution synchrotron X-ray diffraction (SXRD) reveals that $YbMn_xFe_{2-x}O_4$ readily take up oxygen and undergo a structural transition from $R\bar{3}m$ to $P\bar{3}$ to become hyper-stoichiometric $YbMn_xFe_{2-x}O_{4.5}$, which demonstrates their potential as oxygen storage materials. X-ray photoelectron spectroscopy (XPS) implies that Mn^{2+} and Fe^{2+} oxidize to Mn^{3+} and Fe^{3+} after the structural transition. Thermogravimetric analysis (TGA) and *in situ* SXRD measurements at elevated temperatures show that O_2 uptake commences at 200 °C but the structural transition does not until 300 °C. The structural evolution under methane and air, monitored by *in situ* SXRD, implies promising reversibility and structural stability in this series. By performing structural refinements, we find that Mn substitution causes the lattice parameters, a and c, to evolve in a diametric fashion. Strong anisotropic expansion of the lattice occurs in all the reduced phases $YbMn_xFe_{2-x}O_4$ ($R\bar{3}m$) and oxidized phases $YbMn_xFe_{2-x}O_{4.5}$ ($P\bar{3}$). We propose that this phenomenon can be attributed to d-electron filling and crystal field effects for the Mn and Fe cations.

1. Introduction

Oxygen storage materials (OSMs) can take up oxygen into their crystal lattices under oxidation conditions (*e.g.* heating in air) and reversibly release oxygen from their lattices to the environment during reduction (*e.g.* reduction by H_2 or CH_4). In addition to their oxygen storage capacity, OSMs draw great interest in the fields of gas separation,[1–3] fuel combustion efficiency[4–6] and fuel conversion.[7–12] Ideal OSMs should possess proper oxygen releasing/uptake temperature (depending on the application), high oxygen storage capacity, fast oxygen releasing/uptake kinetics, good reversibility, and outstanding mechanical strength during the oxygen release/uptake cycles.[13,14]

The initial and most used OSMs are binary metal oxides with variable-valency transition metal elements, such as Fe_2O_3[15] and Mn_2O_3.[16] However, under oxygen release and uptake cycles, binary oxides undergo extreme structural changes and sintering, thus leading to poor reversibility and mechanical strength.[17] Perovskite oxides with transition metal elements (*e.g.*, $LaFeO_3$) can release/take up oxygen while undergoing minimal crystallographic changes because of their high tolerance of defects.[2] This leaves perovskite oxides with improved reversibility and mechanical strength. The wide tunability of perovskite oxides facilitates the optimization of their properties as OSMs,[1,3,8,18–20] even imparting new functionalities such as catalysis[7] *via* chemical modification.

However, other ternary metal oxides besides perovskites also show promise in the field of OSMs. The hexagonal layered oxide $LnFe_2O_4$, where Ln is a lanthanide cation, and related hexagonal AB_2O_4 materials have recently drawn attention as potential OSMs.[21–23] The crystal structure of $LnFe_2O_4$, given in Fig. 1a, usually adopts $R\bar{3}m$ symmetry[24] and consists of alternating layers of edge-sharing LnO_6 octahedra and edge-sharing FeO_5 trigonal bipyramids. The B site in the structure (Fe in this case) is typically a redox-active transition metal with a mixed valence of +2 and +3. The research interest in $LnFe_2O_4$ and related phases has long focused on their multiferroic properties.[25–30] Both the A and B sites can contain elements with magnetic moments, enabling a magnetic response to an applied external field. The +2 and +3 charges on the B sites undergo charge ordering under certain conditions, leading to the appearance of an electric dipole in the structure (*i.e.* ferroelectric order). The arrangement of the magnetic A site into a triangular lattice also

[a] *Department of Chemistry and Biochemistry, University of Maryland, College Park, Maryland 20742-2115, USA. E-mail: efrain@umd.edu*
[b] *Maryland Quantum Materials Center, University of Maryland, College Park, Maryland 20742, USA*

† Electronic supplementary information (ESI) available. See DOI: 10.1039/d1ma00822f

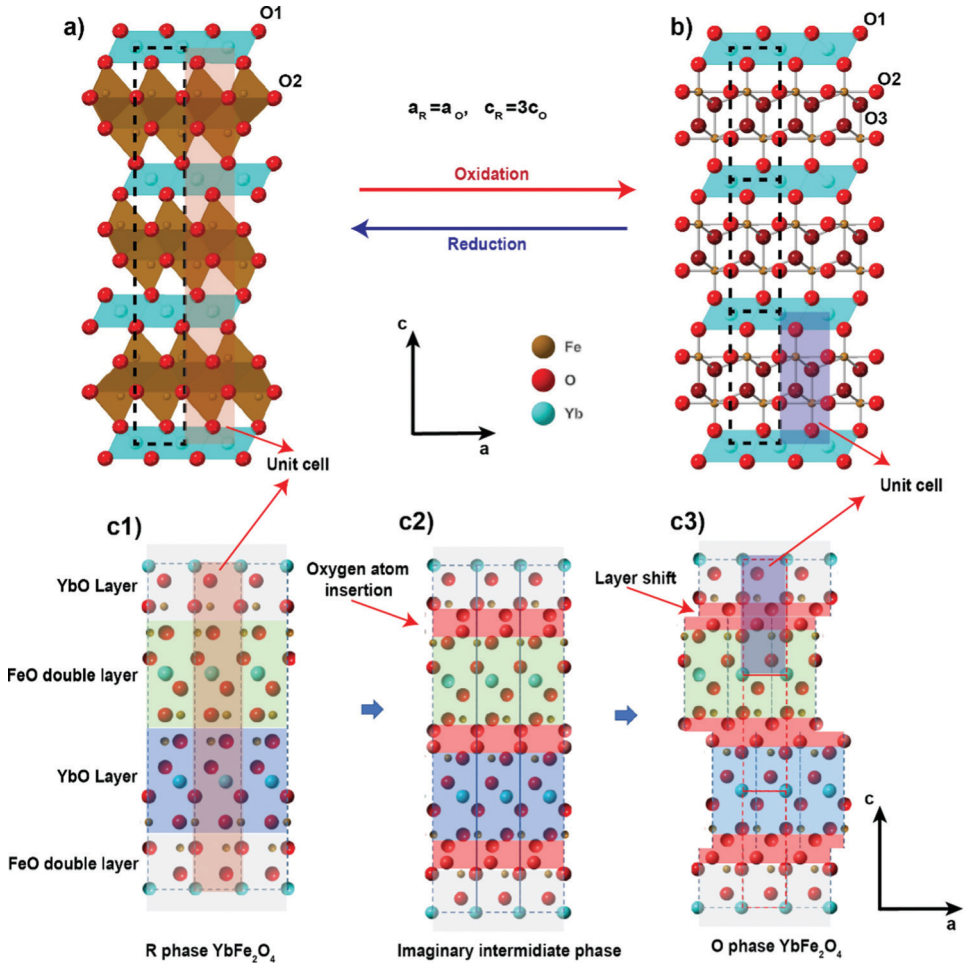

Fig. 1 The crystal structure of (a) $R\bar{3}m$ phase $YbFe_2O_4$ and (b) its oxidized $P\bar{3}$ phase $YbFe_2O_{4.5}$ and (c) the structure relationship between $YbFe_2O_4$ and $YbFe_2O_{4.5}$.

makes the structure a possible frustrated quantum spin liquid system,[31–33] attracting researchers in the field of quantum materials.

Although known for decades that oxygen non-stoichiometry in $LnFe_2O_4$ can tune its physical properties,[34–37] not until recently, was it realized that $LnFe_2O_4$ can take up stoichiometric oxygen into its lattice to become $LnFe_2O_{4.5}$. This accommodation of extra lattice oxygen has the potential to be exploited for oxygen storage applications. Hervieu *et al.* first observed $LuFe_2O_4$ to be oxidized into the hyper-stoichiometric compound $LuFe_2O_{4.5}$ at a relatively low temperature (200 °C) in air.[21] The oxidized phase exhibits a related crystal structure to the original $R\bar{3}m$ phase of $LuFe_2O_4$. Nicou *et al.* first determined the crystal structure of the oxidized phase by studying the oxidation of $YbFe_2O_4$ into $YbFe_2O_{4.5}$.[22] The average crystal structure of the oxidized phase $YbFe_2O_{4.5}$, as solved by Nicoud *et al.*, is presented in Fig. 1b. The new structure adopts trigonal space group $P\bar{3}$ while maintaining the layered arrangement of $LnFe_2O_4$. Our recent work on this system shows that the oxidized phase $LnFe_2O_{4.5}$ (for Ln = Y, In. Lu, Yb) can be reversibly reduced back to $LnFe_2O_4$ by H_2 at 600 °C.[23]

As illustrated in Fig. 1c, the structural relationship between the reduced and oxidized phases of $LnFe_2O_4$ reveals interesting similarities. The slight structural rearrangement between $LnFe_2O_4$ and $LnFe_2O_{4.5}$ leads to high structural reversibility and mechanical strength during the oxidation/reduction cycles. The oxygen storage capacity of $LnFe_2O_4$ (2–3% mass ratio) is comparable to that of most known OSMs.[21–23] More importantly, $LnFe_2O_4$ is highly tolerant towards chemical modifications, much like perovskite oxides. Both A site and B sites can be doped and substituted with abundant elements, bringing huge opportunities to improve their performance as OSMs by chemical modification. Our recent study has already shown that a change of A site elements in AFe_2O_4 can influence the kinetics of the oxidation and reduction during oxygen uptake/releasing cycles.[23]

Here, we conduct B site substitution on the $YbFe_2O_4$. We substitute up to 50% Mn on Fe sites to form a solid solution $YbMn_xFe_{2-x}O_4$ (x = 0.25, 0.50, 0.75, and 1.0). We find that $YbMn_xFe_{2-x}O_4$ readily oxidizes to hyper-stoichiometric $YbMn_xFe_{2-x}O_{4.5}$. We study the influence of Mn substitution on the crystal structure, oxygen uptake behavior, and transition metal oxidation state. We perform cycling experiments on $YbMn_xFe_{2-x}O_4$ in air and a practical fuel, methane. With *in situ* synchrotron X-ray powder diffraction (SXRD), we characterize

the process by which oxygen is incorporated into the crystal lattice. Their structural reversibility reveals their potential as OSMs in applications in fuel combustion and conversion.

We detail the structures of $YbMn_xFe_{2-x}O_4$ and $YbMn_xFe_{2-x}O_{4.5}$ for the first time and observe the effects of B site substitution on lattice expansion. Briefly, Mn-substitution causes the *a*- and *c*-lattice parameters to converge upon incorporating more oxygen. We link such an interesting phenomenon to the change of the electron configuration of the B site element in the triangular bipyramid crystal field between the reduced and oxidized phases. Such lattice properties enable one to potentially engineer the volumetric change during oxidation/reduction cycling, which has practical value for avoiding mechanical failure of OSMs in a fixed-volume reactor.

2. Experiment

2.1 Materials synthesis

$YbMn_xFe_{2-x}O_4$ (x = 1, 0.75, 0.5, and 0.25) series, labeled as the reduced phases or R-phases, were prepared using solid-state reactions. Yb_2O_3, Fe_2O_3, MnO, and Fe powder were ground in $1/2:5/6:(5/3)x:1/3(1-x)$ ratio (x refers to $YbMn_xFe_{2-x}O_4$), respectively, to prepare 0.5 g of the target compound. The powder mixtures were pressed into pellets of 13 mm diameter. The grinding and pelletization were performed in a glove box to prevent the oxidation of Fe powder. The pellets were placed in a 2 mL alumina crucible and sealed inside evacuated 8 mm diameter quartz ampoules. The ampoules were flushed with N_2 gas and evacuated several times to obtain the required oxygen partial pressure for successful synthesis. Typical synthesis of $LnFe_2O_4$ requires P_{O2} below 10^{-7} Torr ($\sim 1.3 \times 10^{-10}$ atm).[38] In our synthesis, the vacuum line we used can reach around 3×10^{-3} Torr ($\sim 4 \times 10^{-6}$ atm) pressure. In order to achieve P_{O2} below 10^{-7} Torr from atmospheric air, N_2 flushing was performed 8–10 times. The samples were sintered at 1180 °C (heating rate 10 °C min^{-1}) for 12 hours and then quenched with ice water. The AB_2O_4 phase is metastable at high temperatures, so we must quench the samples to kinetically trap this phase. Quenching limits the formation of impurities. The elemental ratio of the product was verified with ICP and SEM-EDS. To prepare the oxidized phases, $YbMn_xFe_{2-x}O_{4.5}$, for *ex situ* studies, the as-synthesized samples were oxidized at 600 °C (heating rate 10 °C min^{-1}) in air for 12 h and cooled to room temperature. These samples were labeled as oxidized phases, or O-phases.

2.2 High resolution synchrotron XRD

$YbMn_xFe_{2-x}O_4$ series as well as their oxidized phases $YbMn_xFe_{2-x}O_{4.5}$ were characterized by high-resolution synchrotron X-ray powder diffraction (SXPD). The experiments were performed on the 11-BM beamline at the Advanced Photon Source (APS) at Argonne National Laboratory. X-rays were of wavelength 0.457895 Å. To compare with the SXPD patterns, we also took time-of-flight (TOF) neutron diffraction patterns for the reduced phases $YbMn_xFe_{2-x}O_4$. The TOF patterns were collected on the BL-11A POWGEN beam line at the Spallation Neutron Source (Oak Ridge National Laboratory). Powder patterns were collected at ambient temperature and pressure, and Rietveld analysis was carried out using TOPAS 5[39] and GSASii.[40]

2.3 Thermogravimetric analysis (TGA)

TGA was conducted on reduced phase $YbMn_xFe_{2-x}O_4$ (x = 1, 0.75, 0.5, 0.25) series using an SDT Q600 equipped with a TA Discovery MKS104-S0212004 Micron Vision 2 Mass Spectrometer. 5–10 mg sample was used for each measurement. The samples were heated to 800 °C (ramping rate 10 °C min^{-1}) in air, holding at every 100 °C for 10 minutes. TGA measurements with isotherm heating were also performed. Around 10 mg samples were heated to 350 °C (ramping rate 10 °C min^{-1}) in air and the temperature was held for 6 hours.

2.4 *In situ* synchrotron X-ray diffraction upon heating and cycling with CH_4 and air

We performed *in situ* SXRD experiments (transmission geometry) on $YbMn_xFe_{2-x}O_4$ series (x = 1, 0.75, 0.5, and 0.25) on the 17-BM beamline at the Advanced Photon Source (Argonne National Laboratory). A 2D PerkinElmer a-Si flat panel detector was used with an average wavelength of 0.24108 Å. Two types of experiments were carried out. First, we ramped the temperature of the sample environment up to 700 °C in air, holding at every 100 °C for 10 minutes to determine when $YbMn_xFe_{2-x}O_4$ starts to be oxidized. Second, we performed cycling experiments by switching the atmosphere between air and methane (CH_4) to mimic a practical chemical combustion looping reactor. The samples were heated to 600 °C in He and held at 600 °C while cycling between the two atmospheres (air and methane). A flow-cell/furnace sample holder was used to control the sample temperature and atmosphere.[41] The diffraction patterns were collected every 6s during both processes. Due to the limited beam time, we were not able to collect the cycling data for $YbMn_xFe_{2-x}O_4$ (x = 0.5). Automated sequential Rietveld refinements were performed using TOPAS 5.[39] In the sequential refinement, the position and occupancy of each atom were fixed for simplicity. We monitored the change of lattice parameters as well as the phase fractions. $YbMnFeO_4$ powder samples were characterized by SEM and EDS before and after cycling.

2.5 Valence state determination from X-ray photoelectron spectroscopy (XPS) and X-ray absorption near edge structure (XANES)

Both the reduced $YbMn_xFe_{2-x}O_4$ series and oxidized counterparts were examined by XPS. XPS spectra were collected using a Kratos Axis 165 X-ray photoelectron spectrometer operating in hybrid mode using Al Kα monochromatic X-rays at 280 W. O 1s, Fe 2p, Mn 2p and Yb 4d regions were examined. All XPS spectra were calibrated to the C1s peak at 284.80 eV. All spectra fittings were performed using CasaXPS. Shirley background was used for background subtraction. 30% Gaussian + 70% Lorentzian is applied as the fitted peak shape profile. To further determine the oxidation state of Fe, we performed XANES measurements on $YbMn_{0.25}Fe_{1.5}O_4$ and its oxidized phase. Iron K-edge X-ray

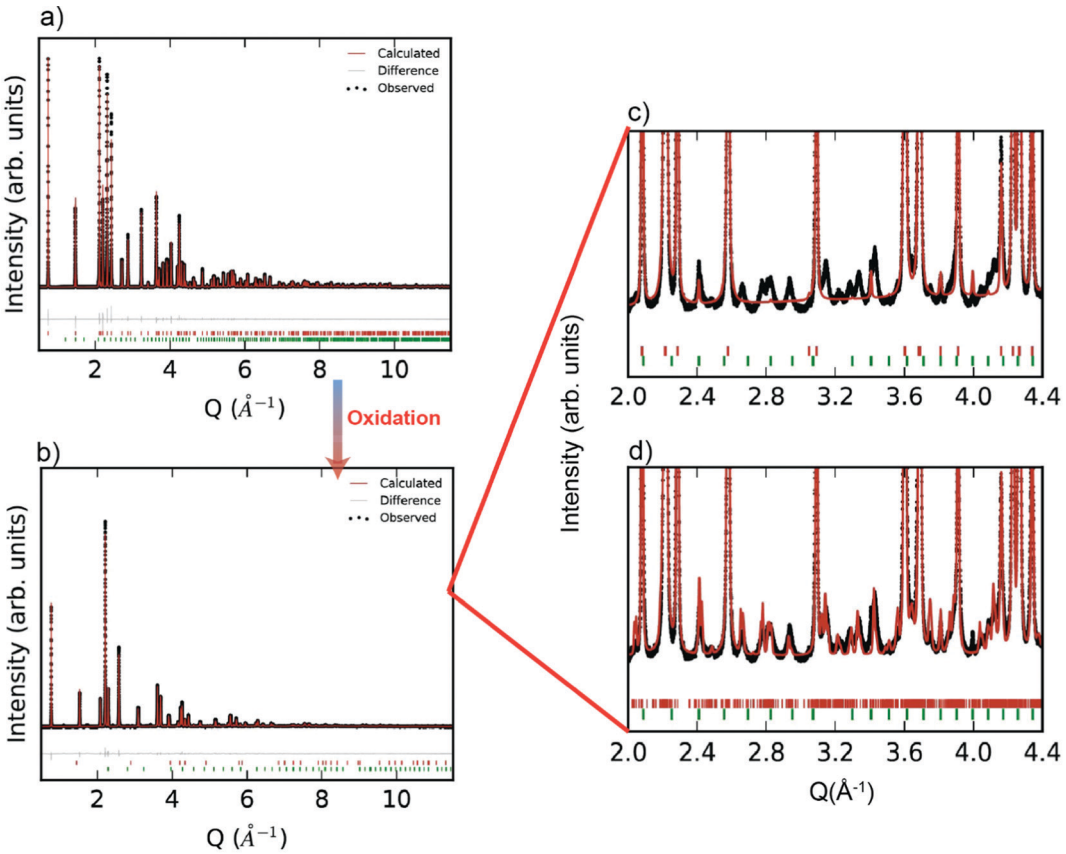

Fig. 2 High-resolution synchrotron X-ray powder diffraction pattern and the Rietveld refinement fit of (a) R-phase $YbMnFeO_4$ and (b) the O phase $YbMnFeO_{4.5}$. R-phase $YbFeMnO_4$ is refined with the $R\bar{3}m$ symmetry and O phase $YbFeMnO_{4.5}$ is refined with the $P\bar{3}$ symmetry. (c) shows the zoomed in region of (b) refined only with the averaged $P\bar{3}$ symmetry while (d) shows the zoomed in region of (b) refined with the incommensurate $P\bar{1}$(abg)0 superspace group. Small amount of Yb_2O_3 exists in the samples (indicated by green tick marks). (c) and (d) are enlarged by 50 times compared with (b).

absorption spectra were collected at beamline 9-BM at the Advanced Photon Source (APS) at Argonne National Laboratory. Measurements were performed in transmission geometry using gas filled ion chambers as detectors on powder samples diluted with boron nitride and pressed into pellets.

3. Results and discussion

3.1 Crystal structure and incommensurate modulation

Room temperature SXRD patterns of the R-phase $YbMn_xFe_{2-x}O_4$ (for $x = 1$) as well as the Rietveld fits to the structures are shown in Fig. 2a. The SXRD patterns of other R-phases $YbMn_xFe_{2-x}O_4$ ($x = 0.75$, 0.5, and 0.25) are presented in the ESI† (Fig. S1a–S3a). The refined parameters are shown in Table S1 (ESI†). All the samples are nearly phase pure with minor impurities of Yb_2O_3(<1%). $YbMnO_3$ (2.3%) and $Yb_2Fe_3O_7$ (1.9%) are also observed in the $YbMn_{0.75}Fe_{1.25}O_4$ ($x = 0.75$) sample. All structures for $YbMn_xFe_{2-x}O_4$ ($x = 1$, 0.75, 0.5, and 0.25) are well modeled by the parent structure of $YbFe_2O_4$ ($R\bar{3}m$ symmetry, Fig. 1a). The observation that Mn substitution on the B-site preserves crystal structure $YbFe_2O_4$ is consistent with the previous reports.[27]

After complete oxidation, the O-phases of $YbMn_xFe_{2-x}O_{4.5}$ can be obtained. The SXRD pattern of $YbMn_xFe_{2-x}O_{4.5}$ ($x = 1$) is displayed in Fig. 2b, and those of the other $YbMn_xFe_{2-x}O_{4.5}$ ($x = 0.75$, 0.5, and 0.25) phases are presented in Figure S1b–S3b (ESI†). In all cases, we observed a crystallographic transition upon oxidation for the SXRD patterns of $YbMn_xFe_{2-x}O_{4.5}$ ($x = 1$, 0.75, 0.5, and 0.25) and we successfully fitted the major Bragg peaks with the $P\bar{3}$ symmetry model, which is reported to be the average crystal structure of unsubstituted $YbFe_2O_{4.5}$[22,23] (Fig. 1b). The final refined structural and lattice parameters are shown in Table S2 (ESI†). The oxygen insertion/uptake in the structure occurs in the Mn/FeO layers, where the O2 and O3 sites are located (Fig. 1c). Thus, the O1 occupancy is fixed to unity and only the occupancies of O2 and O3 are refined. The total occupancies of O2 and O3 are constrained to be 1.25 during refinement to satisfy the oxygen stoichiometry in $YbMn_xFe_{2-x}O_{4.5}$, according to Nicoud *et al.*[22] It is worth noting that besides the major Bragg peaks, we also found an abundance of satellite peaks in all SXRD patterns of the oxidized phases. These satellite peaks are broadly similar for the different samples and cannot be refined with the average $P\bar{3}$ model (Fig. 2c).

Nicoud *et al.*[22] reported a modulated, incommensurate pattern in $YbFe_2O_{4.5}$, which they were able to index and fit by creating a supercell model. By applying a similar superspace group approach, we were able to fit the satellite peaks of the

XRD patterns and observe a decrease of the R_{wp} (Fig. 2d). The modulation parameters are listed in Table S4 (ESI†). A superspace group of $P\bar{1}(abg)0$ and a nearly identical k-vector of (0.141, 0.28, and 0.01) were used for the refinements of all $YbMn_xFe_{2-x}O_{4.5}$ structures. The incommensurate nature of $YbMn_xFe_{2-x}O_{4.5}$ is therefore intrinsic to this system and not a function of the amount of Mn substitution. The incommensurate nature found in $YbMn_xFe_{2-x}O_{4.5}$ may be the result of cation ordering between Fe/Mn. However, Nicoud, S. *et al.* observed similar satellite peaks on the diffraction patterns of $YbFe_2O_{4.5}$ where only Fe exists on the B sites. We conclude that cation ordering is unlikely. Charge ordering is also reported to lead to incommensurate structures in metal oxides. Indeed, charge ordering was extensively studied in $LnFe_2O_4$, but usually appears at a relatively low temperature.[25–30] However, charge ordering does not occur at the temperatures of interest in this study, and there is no possibility of charge order in the fully oxidized phases. Nicoud, S. *et al.* mentioned a possible origin of the incommensurate structure of $YbFe_2O_{4.5}$ deriving from the coexistence of FeO_4, FeO_5, and FeO_6 polyhedra within the $(FeO)_2$ block. Although the average crystal structure shows that Fe atoms are surrounded by 8 closest oxygen atoms, Fe Mössbauer verified the coexistence of FeO_4, FeO_5, and FeO_6 coordination in $LnFe_2O_{4.5}$ systems.[22,34] Based on the fact that Mn substituted series $YbMn_xFe_{2-x}O_{4.5}$ show the same crystal symmetry, and that FeO_4, FeO_5, and FeO_6 polyhedra were also identified in the $LnMnFeO_{4.5}$ (x = 1),[42] we believe that the coexistence of $(Fe, Mn)O_4$, $(Fe, Mn)O_5$, and $(Fe, Mn)O_6$ polyhedra also likely occur in the Mn-substituted series.

Another possible origin for the incommensurate modulation is oxygen vacancy ordering within the $[(Fe, Mn)O]_2$ layer. As shown in Table S2 (ESI†), the oxygen sites O2 and O3 are partially occupied. As presented within the average crystal structure, the distance between the O2 and O3 positions (Fig. 1b) is 2.06–2.14 Å (listed in Table S3, ESI†), which is far below twice the radius of O^{2-} (2.42–2.56 Å).[43,44] Coexistence of O2 and O3 in the same unit cell would imply a highly unstable O–O species in $YbMn_xFe_{2-x}O_{4.5}$, which is unlikely since we observe this phase to be air and water stable at room temperature. Thus, we believe that there is vacancy ordering at the O2 and O3 sites to avoid simultaneous occupation of the O2 and O3 positions. Alternate occupancy of the O2 or O3 positions in one unit cell is consistent with evidence that a Fe/MnO_8 polyhedron is highly unlikely in $YbMn_xFe_{2-x}O_{4.5}$.

3.2 Transition metal oxidation states in the R-phases and O-phases

The transition from $YbMn_xFe_{2-x}O_4$ to $YbMn_xFe_{2-x}O_{4.5}$ involves oxidation of the transition metals. The reduced parent phase $YbFe_2O_4$ is reported to contain 1 : 1 ratio of Fe^{3+} and Fe^{2+}.[22,27] The transition from $YbFe_2O_4$ to $YbFe_2O_{4.5}$ is accompanied by the full conversion of Fe^{2+} to Fe^{3+}.[22] For the reduced phase, $YbMnFeO_4$ (x = 1) is proved to contain Fe^{3+} and Mn^{2+}.[27,45,46] Fig. 3 compares the Fe 2p, Mn 2p, O 1s XPS spectra of $YbMnFeO_4$ (x = 1) to those of the oxidized phase $YbMnFeO_{4.5}$. The Mn $2p_{3/2}$ spectra are strictly fitted following the protocols previously reported,[47] as is presented in Fig. 3b (top). For the reduced phase $YbMnFeO_4$, the Mn $2p_{3/2}$ spectrum is fit satisfactorily with the Mn^{2+} profile. A satellite peak around 646 eV is also characteristic of Mn^{2+}. After oxidation to the O-phase of $YbMnFeO_{4.5}$, we observe a shift of the Mn $2p_{3/2}$ to a higher binding energy and the disappearance of the satellite peak (Fig. 3b bottom). The Mn^{3+} profile can fit the Mn $2p_{3/2}$ spectrum well; we thus conclude that the transition of $YbMnFeO_4$ to $YbMnFeO_{4.5}$ involves the oxidation of Mn^{2+} to Mn^{3+}. The Mn 2p XPS spectra for the rest of the series (x = 0.75, 0.5, and 0.25) are presented in Fig. S5 (ESI†). The oxidation of Mn^{2+} to Mn^{3+} is always observed for the transition from $YbMn_xFe_{2-x}O_4$ to $YbMn_xFe_{2-x}O_{4.5}$.

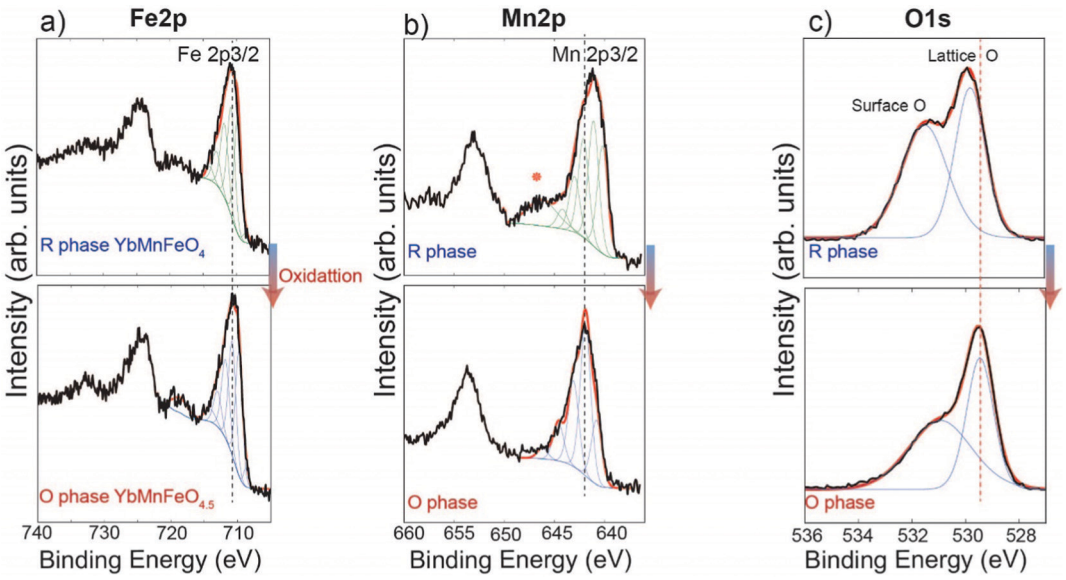

Fig. 3 Comparison of Fe 2p (a), Mn 2p (b) and O 1s (c) XPS spectra between R-phase $YbMnFeO_4$ and the O phase $YbMnFeO_{4.5}$. Upper figures show the spectra from R-phase $YbMnFeO_4$. Lower figures show the spectra from O phase $YbMnFeO_{4.5}$.

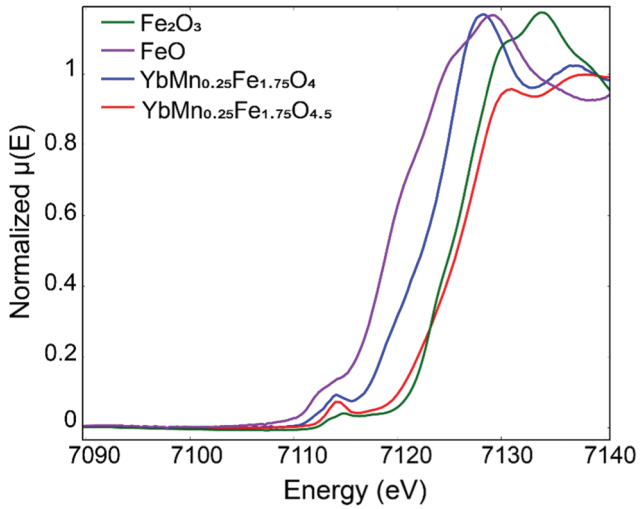

Fig. 4 Fe X-ray absorption near edge structure (XANE) of $YbMn_{0.25}Fe_{1.75}O_4$ and $YbMn_{0.25}Fe_{1.75}O_{4.5}$ in comparison with Fe_2O_3 and FeO reference.

For the Fe $2p_{3/2}$ spectra of $YbMnFeO_4$ ($x = 1$) and $YbMnFeO_{4.5}$, which is presented in Fig. 3a, nearly identical spectra were observed for both reduced and oxidized phases, which can be fitted with the Fe^{3+} profile.[48] It seems to indicate that Fe adopts +3 valence state in both $YbMnFeO_4$ and its oxidized phase $YbMnFeO_{4.5}$. It is unsurprising that reduced phase $YbMnFeO_4$ consists of Fe^{3+} and Mn^{2+} instead of Fe^{2+} and Mn^{3+}, given the stable d^5 configuration of Fe^{3+} and Mn^{2+} cations. A previous magnetic susceptibility study on $YFeMnO_4$ and $YbMnFeO_4$ also indicates the existence of Fe^{3+} and Mn^{2+}.[27,49]

The Fe 2p spectra for the rest of the series ($x = 0.75$, 0.5, and 0.25) are presented in Fig. S4 (ESI†). Theoretically, a mixed Fe^{3+}/Fe^{2+} should exist in the R-phase for bulk samples as long as the Mn substitution ratio is smaller than 1 (*i.e.* $x < 1$) to satisfy charge balancing rules since Mn element exists in the form of Mn^{2+}. However, upon oxidation to form an O-phase, Fe will only exist in the form of Fe^{3+}, similar to what is reported for $YbFe_2O_4/YbFe_2O_{4.5}$,[22] where the valence state of Fe is determined by Mössbauer spectroscopy. Surprisingly, in our XPS measurement, the shape of the Fe spectra remains nearly identical for all the samples before and after oxidation. The determination of the valence state of Fe with XPS still remains challenging as Fe^{3+} and Fe^{2+} spectra heavily overlap. Generally, there should be a characteristic peak around 710 eV for Fe^{2+} 2p spectra,[48] which we did not observe in the R-phase and O-phase. The shape of the Fe $2p_{3/2}$ spectra for both R-phase and O-phase seems to fit with the Fe^{3+} profile, same as the case for $YbMnFeO_4$ to $YbMnFeO_{4.5}$. While we did observe a very slight red shift after oxidation, such a shift does not correspond to the transition from Fe^{2+} to Fe^{3+} (blue shift should be expected) and is very likely caused by the charge compensation due to the different conductivities between the R-phase and O phase.[50,51] The oxidation of Fe^{2+} to Fe^{3+} on the surface in an ambient environment is a common phenomenon for Fe^{2+} containing materials.[48] Since XPS is a surface-sensitive characterization method, we suspect that the Fe^{2+} on the surface of the R-phase $YbMn_xFe_{2-x}O_4$ ($x < 1$) oxidizes to Fe^{3+} due to its instability upon exposure to air.

Apparently XPS here is not suitable for the determination of the valence state of Fe. To prove that mixed Fe^{2+}/Fe^{3+} transforms into Fe^{3+} upon oxidation of $YbMn_xFe_{2-x}O_4$ into $YbMn_xFe_{2-x}O_{4.5}$, we picked $YbMn_{0.25}Fe_{1.75}O_4$ and $YbMn_{0.25}Fe_{1.75}O_{4.5}$ ($x = 0.25$) to perform X-ray absorption near edge structure (XANES) measurements. Fig. 4 depicts the XANES spectra of the reduced and oxidized phases ($x = 0.25$) overlapped with Fe-standards with different oxidation states. As illustrated, the absorption edge of the reduced phase lies in between that of FeO and Fe_2O_3 while the absorption edge of the fully oxidized phase overlaps with that of Fe_2O_3. This confirms that the reduced phase has both Fe^{2+} and Fe^{3+} while the oxidized phase only has Fe^{3+} ions.

Interestingly, we also observe that the binding energy of lattice oxygen systematically shifts to a lower energy from the R-phase to O-phase in the O 1s spectra, as shown in Fig. 3c and Fig. S6 (ESI†). Generally, the lower the binding energy of the oxygen atoms, the more ionic and "free" the oxygen will be in the lattice.[52] This observation implies that the overall oxygen atoms (or anions) in the O-phase $YbMn_xFe_{2-x}O_{4.5}$ may more easily migrate compared to those in the R-phase due to their more ionic nature. This heightened mobility may be attributed to the partial occupation of O2 and O3 sites in the O phase.[53–55] Further studies on ionic conductivity need to be conducted to verify such a hypothesis.

3.3 Oxygen uptake and structure transitions at high temperatures

Characteristic TGA curves in air up to 800 °C, given in Fig. 5, show that the maximum weight gains in $YbMn_xFe_{2-x}O_4$ ($x = 1$, 0.75, 0.5, and 0.25) are within the range of 2–3% (error of 0.5%), which corresponds closely to the theoretical oxygen uptake from $YbMn_xFe_{2-x}O_4$ to $YbMn_xFe_{2-x}O_{4.5}$ (around 2.2% gain for all samples). The TGA curves measured with isotherm heating at 350 °C are displayed in Fig. S7 (ESI†). All samples show around 2.5% mass gains. The theoretical and the measured oxygen storage capacity for each composition are listed in Table S5 (ESI†). The mass gain remains stable after the samples are cooled to room temperature. All the samples start to gain mass when the temperature reaches 200 °C with negligible variances (as shown in Fig. 5 and Fig. S7, ESI†), consistent with what is reported for other $LnFe_2O_4$ materials.[22,23,37]

Apart from TGA, we also performed *in situ* SXRD with the same heating profile as in our TGA measurement in air. We then performed sequential Rietveld refinement on the time-resolved patterns. The *in situ* patterns are shown in Fig. 6. The refined phase composition and lattice parameters *versus* time are displayed in Fig. S8–S11 (ESI†). A clear oxidized phase appears at around 300 °C for all the samples. The kinks at 300 °C shown in TGA curves (Fig. 5) also confirm a phase transition at that temperature. The temperature where new phase appears (300 °C) differs from the temperature where the materials start to gain mass (200 °C), indicating that

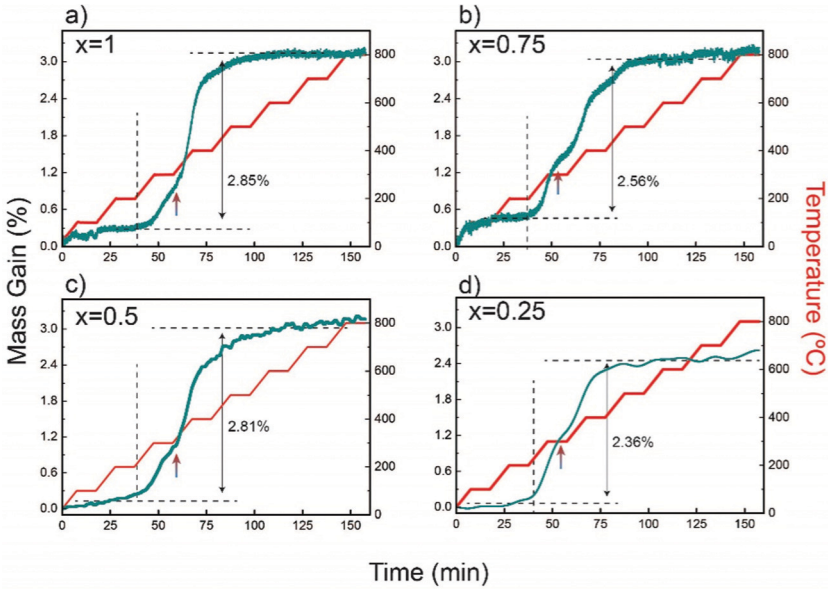

Fig. 5 Thermogravimetric analysis (TGA) depicting the weight change as a function of time and temperature for R-phases $YbMn_xFe_{2-x}O_4$ in air.

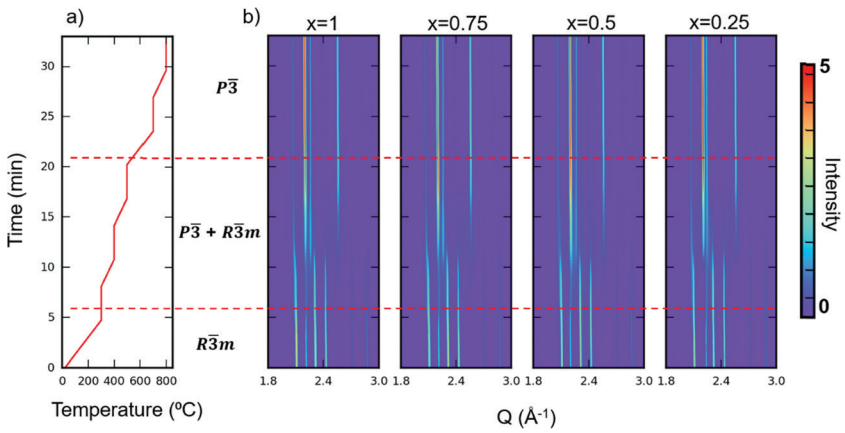

Fig. 6 (a) Heating profile (temperature *vs.* time) of *in situ* characterization of $YbMn_xFe_{2-x}O_4$ and (b) the corresponding contour plots of the SXPD patterns (*vs.* time) when $YbMn_xFe_{2-x}O_4$ is heated in air. The dashed lines separate the regions of $R\bar{3}m$ phases, $R\bar{3}m/P\bar{3}$ mix phases and $P\bar{3}$ phases.

$YbMn_xFe_{2-x}O_4$ series can tolerate some oxygen uptake (around 0.9%) while maintaining its $R\bar{3}m$ structure. The oxygen non-stoichiometry of $LnFe_2O_{4+\delta}$ as the reduced phase ($R\bar{3}m$) has been previously reported and studied.[21,35] In addition, as the time-resolved XRD patterns and refinements show, the phase fraction changes over time, even when the temperature remains constant. Such behavior indicates: (1) the phase transition from the R-phases to O phases is not merely driven by the temperature, and (2) kinetics limits the extent of the observed structural transition, possibly by oxygen diffusion into the lattice.

The TGA and *in situ* heating diffraction measurements imply that the Mn substitution does not have a significant influence on the oxygen uptake and phase transition kinetics, as the oxygen uptake temperature and phase transition temperature for the whole series appear at nearly identical temperatures (200 °C). No significant difference of oxygen uptake kinetics is observed among different Mn substitution levels, as the mass gain saturates at roughly similar temperatures in the isotherm heating measurement (Fig. S7, ESI†).

3.4 Reversible structural evolution during oxygen uptake and release

To examine the reversibility of $YbMn_xFe_{2-x}O_4$ as an oxygen storage material, we performed cycling experiments under oxidizing (air) and reducing (methane) atmospheres. The R-phase samples $YbMn_xFe_{2-x}O_4$ (x = 1,0.75.0.25) were first heated to 600 °C in helium before switching the atmospheres at the same temperature. $YbMn_xFe_{2-x}O_4$ retains the $R\bar{3}m$ structure during the heating in helium, as shown in Fig. S12a (ESI†). For the cycling experiment, the *in situ* time resolved SXRD contour plot of $YbMnFeO_4$ (x = 1) is presented in Fig. 7. The R-phase ($R\bar{3}m$) quickly transitions to the O-phase ($P\bar{3}$) upon

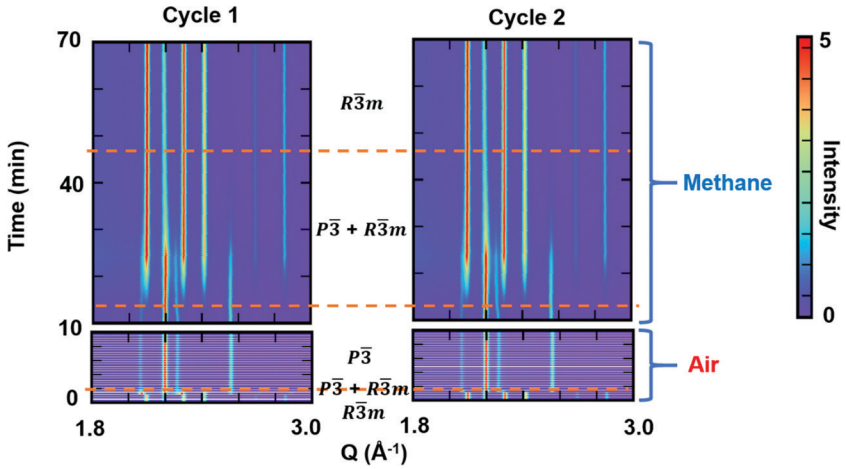

Fig. 7 Contour plots of synchrotron X-ray diffraction patterns of the $YbMnFeO_4$ (x = 1) during cycling between oxidizing (air) and reducing (methane) atmospheres at 600 °C. Two cycles are performed and cycle 1 is followed by cycle 2. Dashed lines separate the regions of $R\bar{3}m$ phase, $R\bar{3}m/P\bar{3}$ mix phases and $P\bar{3}$ phase.

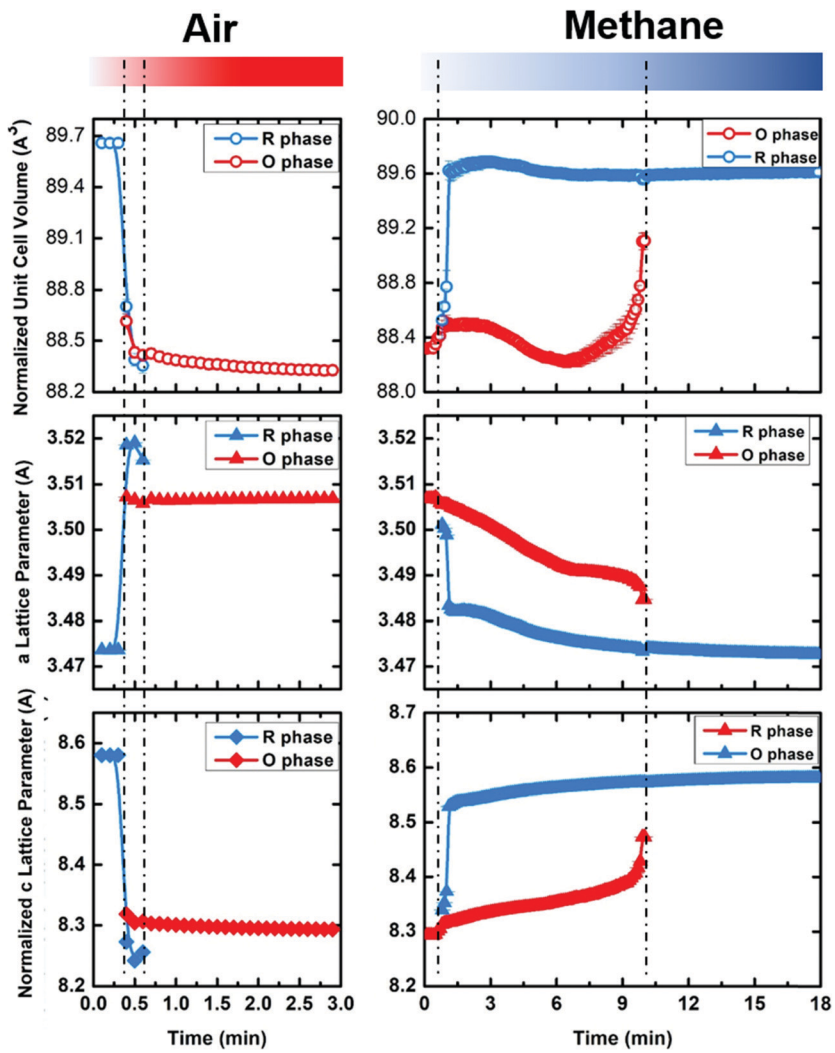

Fig. 8 The evolution of crystal cell volume, a lattice parameter and c lattice parameter as a function of time during cycling between oxidizing (air) and reducing (methane) atmospheres at 600 °C for $YbMnFeO_4$ (x = 1). Note that one unit cell of R-phase corresponds to 3 vertical stacked unit cells of O phase (shown in Fig. 1). Thus, the normalized cell volume and c lattice parameter of the R-phase are used for comparison (1/3 of actual number). The data at 600 °C are extracted from the sequential Rietveld refinement of in-situ synchrotron X-ray diffraction patterns (Fig. 7).

exposure to air. The satellite peaks are still visible in this condition (Fig. S12b, ESI†), implying the stability of the modulated structure in the O-phase. The existence of the satellite peaks in the diffraction patterns also supports that it is not caused by charge ordering as this phenomenon generally appears at relatively low temperatures. Under methane, we observe a much slower transition from the O-phase back to the R-phase. A mixture of phases is visible for a long period under methane before the O-phase finally disappears. Two cycles of experiments were performed, and nearly identical structural evolutions are observed. No obvious new phases are detected and the XRD pattern at the end of cycles is nearly unchanged (Fig. S12c, ESI†), indicating good structural stability and cyclability.

We performed sequential refinements on the diffraction patterns throughout two cycles and extracted phase fractions and lattice parameters. The plot of refined phase fractions for the first cycle, given in Fig. 8a, and for two cycles, shown in Fig. S16 (ESI†), clearly show that both transitions (R → O in air and O → R in methane) are gradual processes, though the oxidation displays much faster kinetics. Fig. S13 (ESI†) plots the refined crystal grain size change in the first oxidation–reduction cycle. It is clear that, during both oxidation and reduction, as the phase fraction changes, the crystal grain size also changes according to whether the phase is growing or contracting. As mentioned earlier, the reaction kinetics may be limited by oxygen ion diffusion into the lattice, such that both oxidation and reduction first occur on the surface and then proceeds to the bulk. Such a mechanism leads to cycling between the growth and contraction of the crystalline size. After the reduction/oxidation cycle the refined crystal size remains nearly unchanged, implying the non-sintering nature of the materials during the cycling. SEM images are also taken before and after the cycling, which is presented in Fig. S14 (ESI†), and no obvious particle size or shape change is observed. EDS elemental mapping (Fig. S15, ESI†) shows that Yb, Mn and Fe are homogenously distributed within the particles before and after the cycling, implying no elemental separation during the cycling and good cycle stability.

Fig. 8b–d present the refined lattice parameters (unit cell volume, *a* and *c*). The transition from the R-phase to O-phase is accompanied by the crystal volume contraction, with elongation in the *a*-direction and contraction in the *c*-direction. We discuss the lattice parameter differences between the R-phase and O-phase in more detail in the next section. Another interesting phenomenon is that the lattice parameters

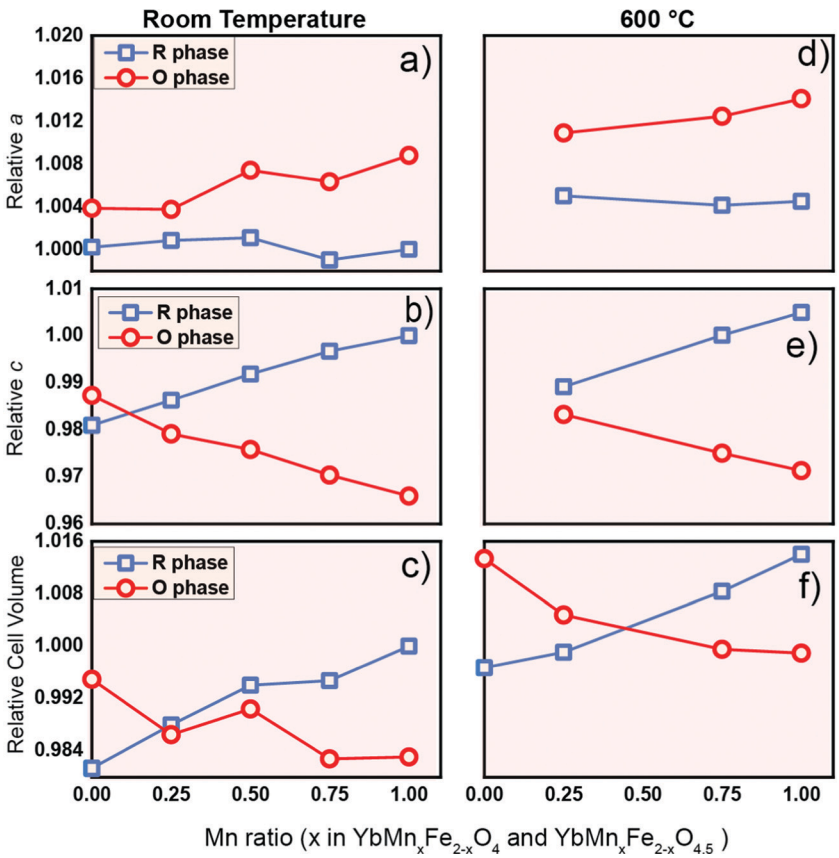

Fig. 9 The Influence of Mn substitution on the lattice parameter *a*, lattice parameter *c* and cell volume of R-phase $YbMn_xFe_{2-x}O_4$ (blue) and the O phase $YbMn_xFe_{2-x}O_{4.5}$ (red) at room temperature (a–c) and 600 °C (d–f). The lattice parameters are normalized. The lattice parameters of R-phase $YbMnFeO_4$ (x = 1) are chosen as references (set as 1). Data for x = 0 ($YbFe_2O_4$ and $YbFe_2O_{4.5}$) from the literature are displayed for comparison.[22,23] *a* and *c* lattice parameters at 600 °C are not listed as the author in the previous literature did not indicate what they were.

for both phases gradually change during cycling. During oxidation of the R-phase, the *a*-lattice parameter grows while the *c*-lattice parameter contracts. During reduction of the O-phase, the opposite occurs. These trends hold before the phase transitions and afterwards during the mixed phase stage. Such lattice parameter changes cannot be attributed to thermal expansion or contraction since the cycling experiments are held at a constant temperature. Thus, it implies that both the R-phase and O-phase can tolerate oxygen non-stoichiometry before phase transitions occur. The R-phase, as is discussed previously, can tolerate some oxygen uptake (around 0.9%) maintaining its rhombohedral structure. The same appears to be true for the O-phase, which can release oxygen from its lattice while keeping its $P\bar{3}$ phase. Due to the very fast material evolution in the cycling and the relative insensitivity of X-rays for oxygen (compared to the metal sites), we were not able to obtain the critical oxygen occupancies for either the R-phases ($R\bar{3}m$) or O-phases ($P\bar{3}$).

Other $YbMn_xFe_{2-x}O_4$ samples (x = 0.75 and 0.25) exhibit similar behavior during the cycling experiments, as displayed in Fig. S17 and S18 (ESI†). The R-phases for both samples cannot be totally converted to the O-phase during the given air exposure time, which is possibly due to the powder packing issue in SXRD quartz tube cells. Nevertheless, both samples undergo reversible structural transitions during switching atmospheres, as the XRD patterns remain nearly identical at the beginning and at the end of the cycles. Our *in situ* cycling experiments show that Mn substitution does not have a significant impact on the oxygen uptake/release reversibility of $YbFe_2O_4$.

3.5 Crystal field effects on lattice volume expansion and contraction

As a potential oxygen storage material, the volume change before and after oxygen release/uptake is a key metric. Large volume expansion and contraction of the material during the cycling can lead to severe mechanical failure of the containers or reactors.[56] Thus, understanding the crystal lattice changes between the reduced phase and oxidized phase is of practical relevance. The relative values of the lattice parameters of the R-phase and O-phase are shown in Fig. 9 at room temperature (Fig. 9a–c) and 600 °C (Fig. 9d–f). All the values for the same lattice parameters are normalized with the corresponding value of the R-phase $YbMnFeO_4$ (x = 1) at room temperature. Data at room temperature are extracted from the refinement of high-resolution SXRD, while the data at 600 °C are extracted from the refinement of *in situ* SXRD during the cycling experiment. We also included the lattice parameters for $YbFe_2O_4$ and $YbFe_2O_{4.5}$ reported elsewhere[22,23] for comparison.

Two interesting trends are worth noting: (1) anisotropic lattice expansion upon oxygen uptake and (2) crystal field effects upon Mn-substitution. For the first trend, we found that all the R-phases take up oxygen into the lattice, and its effect on the *a*- and *c*-lattice parameters occurs in a diametric fashion. Typically, in metal oxides, the attraction between ions is isotropic. For example, the lattice expansion due to the removal of cations from the lattice is commonly reported in the fluorite and perovskite systems.[57,58] In the present series, such lattice expansion is strongly anisotropic. Upon oxidation, if only change of the ionic radius (from Fe^{2+} to Fe^{3+}, and from Mn^{2+} to Mn^{3+}) is taken into consideration, an isotropic expansion should be observed. From the R-phase to O-phase, the *a*-lattice parameter undergoes an expansion while the *c*-lattice parameter significantly contracts. This trend is consistent with the previous study on the $LnFe_2O_4$[22,23] and applies at room temperature as well as at 600 °C. The diametric evolution of the lattice parameters is the result of the crystal structure adjusting to oxygen insertion. As shown in Fig. 1c during the oxidation of the R-phase, oxygen ions insert into the middle of the Fe/MnO double layer; at the same time, the individual Fe/MnO layers shift in opposite directions along the *ab*-plane due to the Coulombic repulsion between oxygen anions. The crowded oxygen ions in the *ab*-direction result in an increased repulsion between each oxygen ion, leading to the expansion of the *a*-parameter.

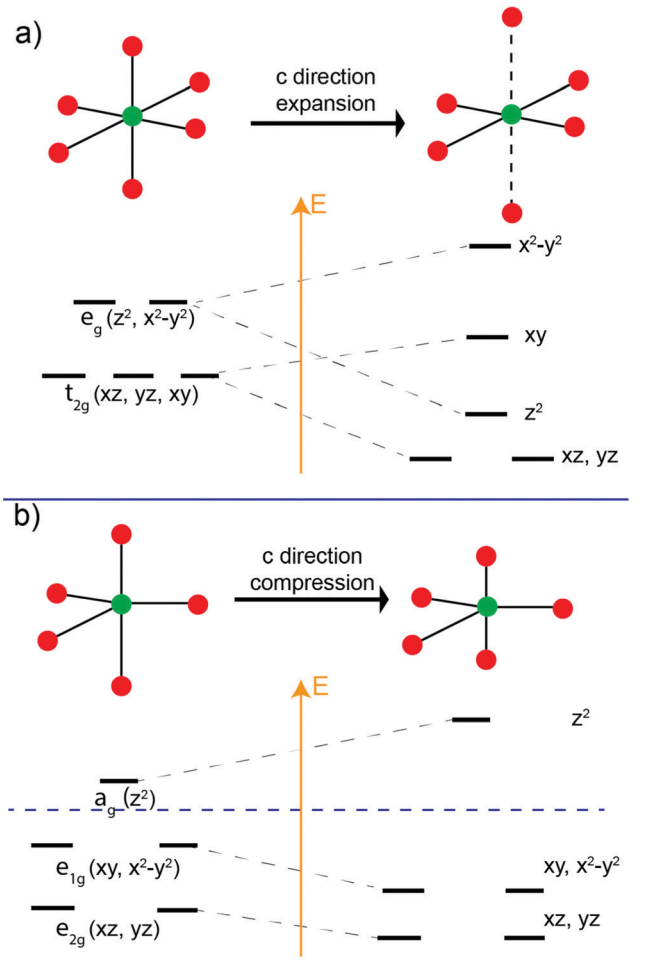

Fig. 10 The influence of *c*-direction distortion on the energy of d orbitals in the (a) octahedral crystal field and (b) trigonal pyramidal crystal field. Distortion leads to rearrangement of d orbitals in the octahedral crystal field system (Jahn Teller effect) and results in a change of relative energy difference of d orbitals in a trigonal pyramidal crystal field.

In the *c*-direction, we observe a contraction because the radius of the Fe^{3+}/Mn^{3+} ion in the oxidized phase is smaller than that of the Fe^{2+}/Mn^{2+} ion in the reduced phase,[44,59] and the extra oxygen ions give rise to the extra attractive force between the oxygen anions and the closest Mn/Fe cations. At room temperature, the degree of the contraction of the *c*-lattice parameter is much larger than the expansion in the *a*-direction. The normalized crystal cell volume of the R-phase is therefore always larger than that of the O-phase (Fig. 9c), consistent with the *c*-lattice parameter trend. At a certain point of Mn-substitution, however, we observe that the unit cell volume values intersect at 600 °C (Fig. 9f). This crossover point implies that the amount of Mn-substitution affects the thermal expansion of the lattice.

The second interesting trend is that Mn substitution has an opposite influence on the lattice parameters of the R-phases and O-phases. For the R-phase (blue line) in Fig. 9a and b, we can observe that the increase of the Mn substitution level leads to the contraction in the *a*-direction but an expansion along the *c*-direction. Contrastingly, for the O-phase (red line) as shown in Fig. 9a and 9b, an increase of Mn-substitution causes the expansion along the *a*-direction and contraction along the *c*-direction. We term this phenomenon a "double distortion" effect of Mn-substitution on the crystal structure. Practically, it leads to an enlarged gap between the lattice parameters of R-phases and O-phases as the Mn-substitution level increases.

The "double distortion" effect cannot be simply explained by the different ionic radii of the cations since the influence of Mn substitution is very anisotropic in this system. Therefore, what is the real driving force for the opposite impact of Mn-substitution? In short, we hypothesize that the distortions result from the crystal field effects. Even though the Fe/MnO_5 bipyramidal bilayer in the R-phases becomes more complex after oxidation into the O-phase, the same bipyramidal polyhedra exist in both phases.[22] We propose that in the bipyramidal crystal field, different *d*-electron fillings of Mn^{2+}/Fe^{2+} in the R-phase and Mn^{3+}/Fe^{3+} in the O-phase lead to the diametric and strongly anisotropic influence of Mn- substitution on the crystal structure.

It is well known that for octahedral crystal fields (ideal point group O_h), if the metal center is Jahn–Teller active (*e.g.* d^2, d^4), the ML_6 octahedron will undergo an anisotropic distortion to lower the O_h symmetry. The distortion lifts the energy-level degeneracy of the d-orbital manifold, and the electron filling occurs so the energy of the system is lowered in the newly modified crystal field[60,61] (Fig. 10a). We believe that a similar phenomenon occurs in our Fe/MnO trigonal bipyramidal systems.

In the trigonal bipyramidal crystal field, compression or elongation along the *c*-direction does not change the site symmetry (*e.g.* D_{3h}, C_{3v}). Unlike the case for octahedral coordination, such distortions for trigonal bipyramids do not lead to the rearrangement of d-orbital energy levels. However, the relative energy level of the d-orbitals can be significantly

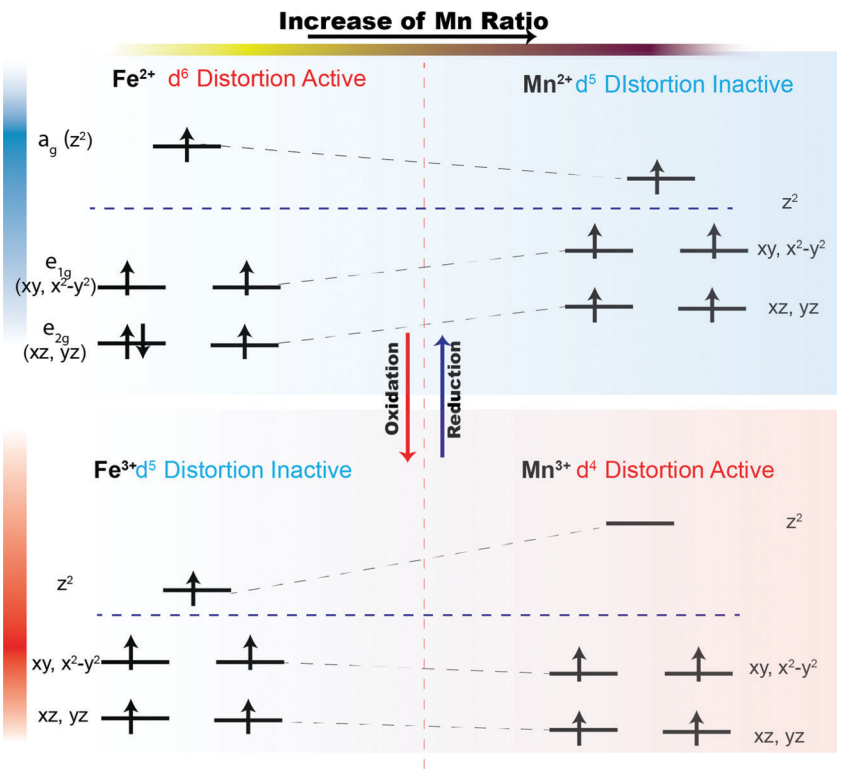

Fig. 11 Illustration of how Mn substitution influences the trigonal pyramidal crystal field R-phase $YbMn_xFe_{2-x}O_4$ and the O phase $YbMn_xFe_{2-x}O_{4.5}$. In R-phase $YbMn_xFe_{2-x}O_4$, Mn substitution leads to the replacement of Fe^{2+} (d^6) by Mn^{2+} (d^5). However, in O phase $YbMn_xFe_{2-x}O_{4.5}$, Mn substitution leads to the replacement of Fe^{3+} (d^5) by Mn^{3+} (d^4).

modified. As is illustrated in Fig. 10b, in the trigonal bipyramidal field, compression in the *c*-direction increases the energy level of the a_g (d_{z^2}) orbital while those of the doubly degenerate e_{1g} (d_{xy}, $d_{x^2-y^2}$) and e_{2g} (d_{xz}, d_{yz}) decrease so that the total orbital energy of the system does not the change.

For the trigonal bipyramidal $(Mn,Fe)O_5$ polyhedra in the present series, the electron count will determine whether a compressed crystal field will lower the total energy of the systems. The influence of Mn^{2+}, Fe^{2+}, Mn^{3+}, and Fe^{3+} in the MO_5 trigonal bipyramidal polyhedron crystal field is presented in Fig. 11. We assume that the metal ions in the MO_5 trigonal bipyramids always adopt a high spin configuration. In the R-phase, Mn^{2+} has a d^5 electron configuration and all orbitals are singly occupied. Therefore, the compression of the trigonal bipyramids has no effect on the total energy of the system. In the case of Fe^{2+}, the d^6 electron configuration leads to an extra electron in the e_{2g} manifold, and the total energy of the system will be lowered if the trigonal bipyramids are compressed. Thus, we term Fe^{2+} is "distortion-active" while Mn^{2+} is "distortion-inactive". As the level of Mn-substitution increases, the MO_5 polyhedra will be less compressed, resulting in an expansion along the *c*-direction and contraction in the *ab*-plane for the R-phase. Conversely, in the O-phase, Mn^{3+} has a d^4 electron configuration and the a_g orbital is therefore empty. Compression of the trigonal bipyramids significantly lowers the energy of the electrons in the e_{1g} (d_{xy}, $d_{x^2-y^2}$) and e_{2g} (d_{xz}, d_{yz}) levels. Mn^{3+} is therefore "distortion-active" whereas Fe^{3+} with its d^5 electron configuration is "distortion-inactive". Increasing the Mn-substitution in the O-phase favors the compression of MO_5 polyhedra, causing the contraction along the *c*-direction and expansion in the *ab*-plane. Therefore, we have an explanation for the 'double distortion' effect observed in the lattice parameter evolution by considering whether the phase includes distortion-active or distortion-inactive cations.

In addition to lattice parameters, we can also follow the metal–oxygen interatomic distances from diffraction data to understand this crystal field-driven distortion. Fig. 12 shows the influence of Mn substitution on the Mn/Fe–O bond distances in the R-phases and O-phases. As the Mn-substitution level increases in the R-phases, the Mn/Fe–O bond distances along the *c*-direction expand while the bond distances in the *ab*-plane contract. The opposite trend occurs in the O-phases. These trends of metal–oxygen bond distances along different directions are consistent with our hypothesis regarding the MO_5 trigonal crystal fields. The influence of Mn^{3+} and Fe^{3+} on the lattice parameters in the MO_5 trigonal bipyramidal polyhedron is also reported in the hexagonal $LnMn_{1-x}Fe_xO_3$ (Ln = Y, Lu, Yb).[62–64] Similar to our O-phase, the hexagonal $LnMn_{1-x}Fe_xO_3$ system displays a decrease in the

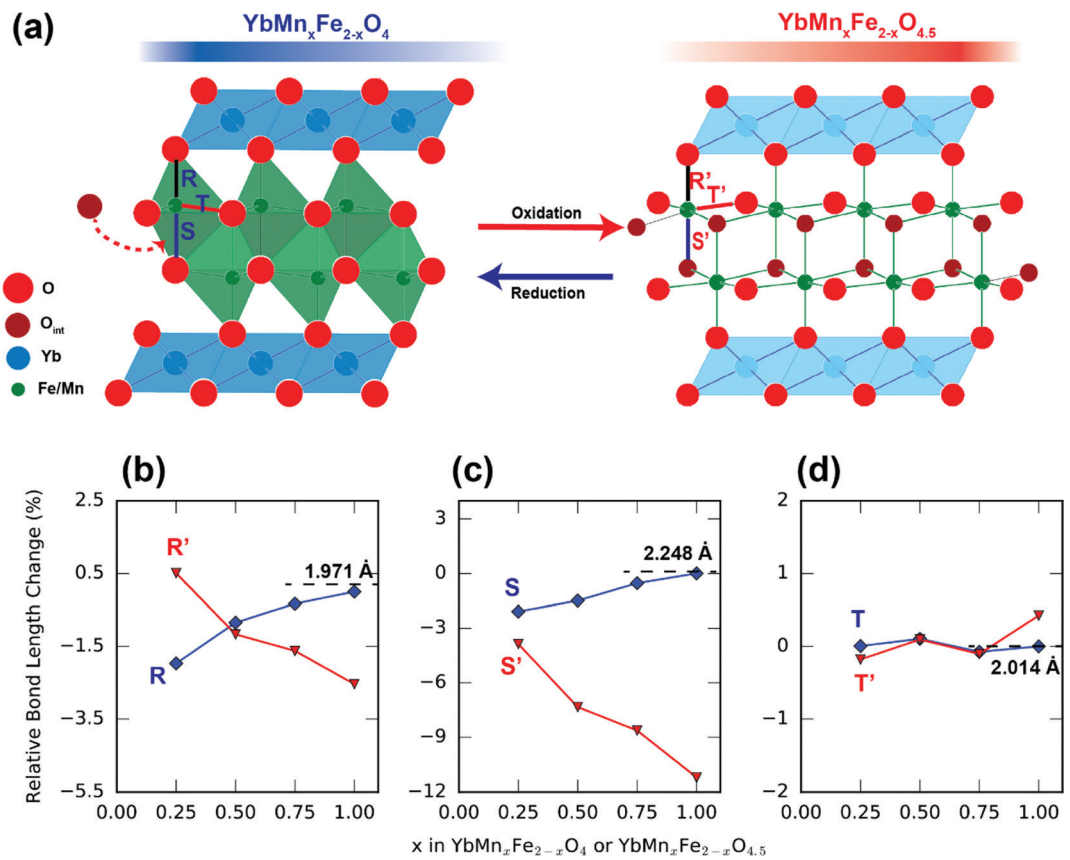

Fig. 12 Influence of Mn substitution on different Fe/Mn–O bond lengths of R-phase $YbMn_xFe_{2-x}O_4$ (blue) and the O phase $YbMn_xFe_{2-x}O_{4.5}$ (red). The bonds labeled as R/R′ (b), S/S′ (c) and T/T′ (d) are indicated in Fig. 12a. The bond lengths are normalized. The bond lengths of R-phase $YbMn_xFe_{2-x}O_4$ (x = 1) are chosen as references (set as 1, change as 0%).

Fe/Mn–O bonds along the *c*-direction and an increase in the *ab*-plane as the Mn ratio increases.

Outside the present system, it is quite rare in metal oxides to observe Mn^{2+} and Fe^{2+} in MO_5 trigonal bipyramidal coordination. Therefore, it is instructive to examine cases of analogous molecular complexes. Pritchard *et al.* reported the existence of $M^{2+}L_5$ trigonal bipyramidal polyhedra in $[M(II)Cl_3(Hdabco)(dabco)]_n$ and $[M(II)Cl_3(HdabcoH)_2]$ complexes where dabco = 1,4-diazabicyclo[2.2.2]-octane. In these complexes, the M^{2+} coordinates to three Cl^- ions in the equatorial plane and two N atoms of the ligand in the apical position. Upon exchanging Mn^{2+} by Fe^{2+}, the M—Cl bond elongates while the M—N bond shortens the bond,[65] which is consistent with our observation on the influence of Mn on the M–O bonds in R-phases. To our knowledge, we are the first to observe here a reversible valence change of ML_5 trigonal bipyramids leading to a diametric effect on the lattice parameters.

The change in the Mn/FeO layer also slightly impacts the presumably rigid YbO layer itself. The expansion of the Mn/FeO layer applies a force on the neighboring YbO layer, driving it to be compressed, even though it remains chemically unchanged by the Mn-substitution. As presented in Fig. S19 (ESI†), the Yb–O bond length grows in the O-phase while it decreases in the R-phases with increasing Mn-substitution. This trend is consistent with that of the *a*-lattice parameter.

4. Conclusion

In summary, like their parent structure, the Mn-substituted R-phases show promising performance as oxygen storage materials. All $YbMn_xFe_{2-x}O_4$ compositions studied here readily take up oxygen at relatively low temperatures and undergo a phase transition to the O-phases; $YbMn_xFe_{2-x}O_{4.5}$, Mn-substitution does not lead to a separate phase transition for either R-phase $YbMn_xFe_{2-x}O_4$ or O-phase $YbMn_xFe_{2-x}O_{4.5}$. R-phases adopt $R\bar{3}m$ symmetry while the average crystal structure phase of the O-phase is $P\bar{3}$. All display a complex incommensurate modulation (superspace group $P\bar{1}$(abg)0), indicative of ordering of MO_n polyhedra for n = 4, 5, and 6. Our *in situ* diffraction studies indicate that the oxygen uptake temperature and the reaction kinetics are not greatly impacted by the Mn substitution. In addition, all $YbMn_xFe_{2-x}O_4$ can reversibly transit between R-phases and O-phases in the alternative air and methane environment, showing their great cycling stability and potential to be applied in fuel combustion and conversion as OSMs.

Interestingly, in this system with reversible phase transitions driven by oxidation, the change in the d-electron configuration dictates the lattice expansion properties. The effect on the diverging *a*- and *c*-lattice parameters was termed a ''double distortion'' effect and we hypothesize that it is derived by crystal field effects in this system. The change from Mn^{2+}/Fe^{2+} to Mn^{3+}/Fe^{3+} in the MO_5 trigonal bipyramidal causes a switch in which the metal ion is the 'distortion-active' ion. Because of the switching of roles upon oxygen release and uptake (*e.g.* Mn^{3+} is distortion-active whereas Mn^{2+} is not), the Mn-substitution leads to opposite influences on the lattice parameters of the R-phases and O-phases. This tuning of the lattice volume changes with Mn-substitution could be exploited to minimize the volume changes upon using this system as an OSM.

Conflicts of interest

There are no conflicts to declare.

Acknowledgements

We acknowledge the Department of Commerce/NIST award 70NANB17H301 for support. Use of the Advanced Photon Source at Argonne National Laboratory was supported by the U.S. Department of Energy, Office of Science, Office of Basic Energy Sciences, under Contract No. DE-AC02-06CH11357. We thank W. Xu and A. Yakovenko at 17 BM, ANL, for their help with SXRD data collection. We thank Dr Sterbinsky at the 9-BM for XAS data collection. A portion of this research used resources at the Spallation Neutron Source, a DOE Office of Science User Facility operated by the Oak Ridge National Laboratory. We thank M. Kirkham and C. Li at POWGEN, SNS, ORNL for their help with powder neutron diffraction experiments.

References

1 A. Klimkowicz, T. Hashizume, K. Cichy, S. Tamura, K. Świerczek, A. Takasaki, T. Motohashi and B. Dabrowski, *J. Mater. Sci.*, 2020, **55**, 15653–15666.
2 J. Vieten, B. Bulfin, F. Call, M. Lange, M. Schmücker, A. Francke, M. Roeb and C. Sattler, *J. Mater. Chem. A*, 2016, **4**, 13652–13659.
3 J. Vieten, B. Bulfin, D. E. Starr, A. Hariki, F. M. F. de Groot, A. Azarpira, C. Zachäus, M. Hävecker, K. Skorupska, N. Knoblauch, M. Schmücker, M. Roeb and C. Sattler, *Energy Technol.*, 2019, **7**, 131–139.
4 Q. Imtiaz, A. Kurlov, J. L. M. Rupp and C. R. Müller, *ChemSusChem*, 2015, **8**, 2055–2065.
5 H. Thunman, F. Lind, C. Breitholtz, N. Berguerand and M. Seemann, *Fuel*, 2013, **113**, 300–309.
6 H. Falcón, J. A. Barbero, J. A. Alonso, M. J. Martínez-Lope and J. L. G. Fierro, *Chem. Mater.*, 2002, **14**, 2325–2333.
7 X. Zhu, K. Li, L. Neal and F. Li, *ACS Catal.*, 2018, **8**, 8213–8236.
8 L. Zhang, L. Zhang, Y. Hu, Y. Hu, W. Xu, W. Xu, C. Huang, Y. Su, M. Tian, Y. Zhu, H. Gong and X. Wang, *Energy Fuels*, 2020, **34**, 6991–6998.
9 X. P. Dai, R. J. Li, C. C. Yu and Z. P. Hao, *J. Phys. Chem. B*, 2006, **110**, 22525–22531.
10 I. S. Metcalfe, B. Ray, C. Dejoie, W. Hu, C. de Leeuwe, C. Dueso, F. R. García-García, C. M. Mak, E. I. Papaioannou, C. R. Thompson and J. S. O. Evans, *Nat. Chem.*, 2019, **11**, 638–643.
11 X. Zhu, Q. Imtiaz, F. Donat, C. R. Müller and F. Li, *Energy Environ. Sci.*, 2020, **13**, 772–804.
12 Y. Liu, L. Qin, Z. Cheng, J. W. Goetze, F. Kong, J. A. Fan and L. S. Fan, *Nat. Commun.*, 2019, **10**, 1–6.

13 J. Adánez, L. F. De Diego, F. García-Labiano, P. Gayán, A. Abad and J. M. Palacios, *Energy Fuels*, 2004, **18**, 371–377.
14 J. Adanez, A. Abad, F. Garcia-Labiano, P. Gayan and L. F. De Diego, *Prog. Energy Combust. Sci.*, 2012, **38**, 215–282.
15 H. A. Alalwan, S. E. Mason, V. H. Grassian and D. M. Cwiertny, *Energy Fuels*, 2018, **32**, 7959–7970.
16 Q. Zafar, T. Mattisson and B. Gevert, *Ind. Eng. Chem. Res.*, 2005, **44**, 3485–3496.
17 J. Zieliński, I. Zglinicka, L. Znak and Z. Kaszkur, *Appl. Catal., A*, 2010, **381**, 191–196.
18 D. D. Taylor, N. J. Schreiber, B. D. Levitas, W. Xu, P. S. Whitfield and E. E. Rodriguez, *Chem. Mater.*, 2016, **28**, 3951–3960.
19 T. Li, R. S. Jayathilake, D. D. Taylor and E. E. Rodriguez, *Chem. Commun.*, 2019, **55**, 4929–4932.
20 A. Demizu, K. Beppu, S. Hosokawa, K. Kato, H. Asakura, K. Teramura and T. Tanaka, *J. Phys. Chem. C*, 2017, **121**, 19358–19364.
21 M. Hervieu, A. Guesdon, J. Bourgeois, E. Elkaïm, M. Poienar, F. Damay, J. Rouquette, A. Maignan and C. Martin, *Nat. Mater.*, 2014, **13**, 74–80.
22 S. Nicoud, M. Huvé, O. Hernandez, A. Pautrat, M. Duttine, A. Wattiaux, C. Colin, H. Kabbour and O. Mentré, *J. Am. Chem. Soc.*, 2017, **139**, 17031–17043.
23 R. S. Jayathilake, B. D. Levitas and E. E. Rodriguez, *J. Mater. Chem. A*, 2018, **6**, 4801–4810.
24 N. Kimizuka, A. Takenaka, Y. Sasada and T. Katsura, *Solid State Commun.*, 1974, **15**, 1321–1323.
25 A. Nagano and S. Ishihara, *J. Phys.: Condens. Matter*, 2007, **19**, 5.
26 C. R. Serrao, J. R. Sahu, K. Ramesha and C. N. R. Rao, *J. Appl. Phys.*, 2008, **104**, 016102.
27 K. Yoshii, N. Ikeda, T. Michiuchi, Y. Yokota, Y. Okajima, Y. Yoneda, Y. Matsuo, Y. Horibe and S. Mori, *J. Solid State Chem.*, 2009, **182**, 1611–1618.
28 Y. Sun, Y. Liu, F. Ye, S. Chi, Y. Ren, T. Zou, F. Wang and L. Yan, *J. Appl. Phys.*, 2012, **111**, 07D902.
29 A. D. Christianson, M. D. Lumsden, M. Angst, Z. Yamani, W. Tian, R. Jin, E. A. Payzant, S. E. Nagler, B. C. Sales and D. Mandrus, *Phys. Rev. Lett.*, 2008, **100**, 107601.
30 A. J. Hearmon, D. Prabhakaran, H. Nowell, F. Fabrizi, M. J. Gutmann and P. G. Radaelli, *Phys. Rev. B: Condens. Matter Mater. Phys.*, 2012, **85**, 014115.
31 Y. Shen, Y. D. Li, H. C. Walker, P. Steffens, M. Boehm, X. Zhang, S. Shen, H. Wo, G. Chen and J. Zhao, *Nat. Commun.*, 2018, **9**, 1–7.
32 J. A. M. Paddison, M. Daum, Z. Dun, G. Ehlers, Y. Liu, M. B. Stone, H. Zhou and M. Mourigal, *Nat. Phys.*, 2017, **13**, 117–122.
33 Y. Li, *Adv. Quantum Technol.*, 2019, **2**, 1900089.
34 I. Nodari, A. Alebouyeh, J. F. Brice, R. Gérardin and O. Evrard, *Mater. Res. Bull.*, 1988, **23**, 1039–1044.
35 S. Cao, J. Lee, Z. Wang, H. Tian, Y. Qin, L. Zeng, C. Ma, H. Yang and J. Li, *Sci. Rep.*, 2012, **2**, 1–4.
36 J. Akimitsu, Y. Inada, K. Siratori, I. Shindo and N. Kimizuka, *Solid State Commun.*, 1979, **32**, 1065–1068.
37 F. Wang, J. Kim, G. D. Gu, Y. Lee, S. Bae and Y. J. Kim, *J. Appl. Phys.*, 2013, **113**, 063909.
38 C. M. Brooks, R. Misra, J. A. Mundy, L. A. Zhang, B. S. Holinsworth, K. R. O'Neal, T. Heeg, W. Zander, J. Schubert, J. L. Musfeldt, Z. K. Liu, D. A. Muller, P. Schiffer and D. G. Schlom, *Appl. Phys. Lett.*, 2012, **101**, 132907.
39 R. W. Cheary and A. Coelho, *J. Appl. Crystallogr.*, 1992, **25**, 109–121.
40 B. H. Toby and R. B. Von Dreele, *J. Appl. Crystallogr.*, 2013, **46**, 544–549.
41 P. J. Chupas, K. W. Chapman, C. Kurtz, J. C. Hanson, P. L. Lee and C. P. Grey, *J. Appl. Crystallogr.*, 2008, **41**, 822–824.
42 O. E. R. Gerardin, H. Aqachmar, I. Nodari and J. FBrich, *J. Phys. Chem. Solids*, 1989, **50**, 43–48.
43 L. Pauling, *J. Am. Chem. Soc.*, 1931, **53**, 1367–1400.
44 L. H. Ahrens, *Geochim. Cosmochim. Acta*, 1952, **2**, 155–169.
45 M. Nespolo, M. Isobe, J. Iida and N. Kimizuka, *Acta Crystallogr., Sect. B: Struct. Sci.*, 2000, **56**, 805–810.
46 A. G. Gamzatov, A. M. Aliev, M. N. Markelova, N. A. Burunova, A. R. Kaul', A. S. Semisalova and N. S. Perov, *Phys. Solid State*, 2016, **58**, 1143–1147.
47 M. C. Biesinger, B. P. Payne, A. P. Grosvenor, L. W. Lau, A. R. Gerson and R. S. C. Smart, *Appl. Surf. Sci.*, 2011, **257**, 2717–2730.
48 A. P. Grosvenor, B. A. Kobe, M. C. Biesinger and N. S. McIntyre, *Surf. Interface Anal.*, 2004, **36**, 1564–1574.
49 I. Junji, T. Midori and N. Yasuaki, *J. Phys. Soc. Jpn.*, 2013, **59**, 4443–4448.
50 J. B. Metson, *Surf. Interface Anal.*, 1999, **27**, 1069–1072.
51 J. Cazaux, *J. Electron Spectrosc. Relat. Phenom.*, 2000, **113**, 15–33.
52 L. Q. Wu, Y. C. Li, S. Q. Li, Z. Z. Li, G. D. Tang, W. H. Qi, L. C. Xue, X. S. Ge and L. L. Ding, *AIP Adv.*, 2015, **5**, 97210.
53 D. Y. Wang, D. S. Park, J. Griffith and A. S. Nowick, *Solid State Ionics*, 1981, **2**, 95–105.
54 T. L. Nguyen, M. Dokiya, S. Wang, H. Tagawa and T. Hashimoto, *Solid State Ionics*, 2000, **130**, 229–241.
55 R. A. De Souza, A. Ramadan and S. Hörner, *Energy Environ. Sci.*, 2012, **5**, 5445–5453.
56 S. Jašo, H. Arellano-Garcia and G. Wozny, *A Novel Design Concept for the Oxidative Coupling of Methane Using Hybrid Reactors*, Elsevier, 2011, vol. 29.
57 D. Marrocchelli, N. H. Perry and S. R. Bishop, *Phys. Chem. Chem. Phys.*, 2015, **17**, 10028–10039.
58 Y. Wang, K. Duncan, E. D. Wachsman and F. Ebrahimi, *Solid State Ionics*, 2007, **178**, 53–58.
59 L. Pauling, *Nature of the Chemical Bond*, 3rd edn, 1960, vol. 17, pp. 505–562.
60 H. A. Jahn and E. Teller, *Stability of Polyatomic Molecules in Degenerate Electronic States I. Orbital Degeneracy*, 1968.
61 H. A. Jahn and E. Teller, *Proc. R. Soc. London, Ser. A*, 1937, **161**, 220–235.
62 S. L. Samal, T. Magdaleno, K. V. Ramanujachary, S. E. Lofland and A. K. Ganguli, *J. Solid State Chem.*, 2010, **183**, 643–648.
63 S. L. Samal, W. Green, S. E. Lofland, K. V. Ramanujachary, D. Das and A. K. Ganguli, *J. Solid State Chem.*, 2008, **181**, 61–66.
64 J. G. Lin, Y. S. Chen and T. C. Han, *J. Appl. Phys.*, 2010, **107**, 09D902.
65 R. G. Pritchard, M. Ali, A. Munim and A. Uddin, *Acta Crystallogr., Sect. C: Cryst. Struct. Commun.*, 2006, **62**, 507–509.